

PFC/JA-85-31

EFFECT OF PELLET FUELING ON ENERGY TRANSPORT  
IN OHMICALLY HEATED ALCATOR C PLASMAS

S.M. Wolfe, M. Greenwald, R. Gandy, R. Granetz,  
C. Gomez, D. Gwinn, B. Lipschultz, S. McCool,  
E. Marmor, J. Parker, R.R. Parker, J. Rice

September, 1985

Plasma Fusion Center  
Massachusetts Institute of Technology  
Cambridge, MA 02139

This work was supported by the U.S. Department of Energy Contract No. DE-AC02-78ET51013. Reproduction, translation, publication, use and disposal, in whole or in part by or for the United States government is permitted.

Submitted for publication in: Nuclear Fusion

**EFFECT OF PELLET FUELING ON ENERGY TRANSPORT  
IN OHMICALLY HEATED ALCATOR C PLASMAS**

**S.M.WOLFE, M.GREENWALD, R.GANDY\*, R.GRANETZ,  
C.GOMEZ, D.GWINN, B.LIPSCHULTZ, S.MCCOOL†,  
E.MARMAR, J.PARKER‡, R.R.PARKER, J.RICE**

*Plasma Fusion Center, M.I.T.  
Cambridge, Massachusetts, U.S.A.*

**Abstract**

We have carried out time-dependent transport analysis calculations using experimentally determined plasma parameters to obtain the variation of electron and ion thermal diffusivities following pellet injection into moderate density ALCATOR C discharges. The ion thermal diffusivity, which is typically higher than neoclassical predictions by a factor of four in the gas fueled target plasma, is found to decrease following injection to approximately the neoclassical value. The electron thermal conductivity is not reduced following injection. The improvement in ion transport correlates with the peaking of the density profile and may be related to the reduction in the quantity  $dl_n T_i/dl_n n$  in the pellet fueled case. Extrapolation of these results to higher density plasmas, for which the electron and ion losses cannot be unambiguously measured, is consistent with previously reported increases in global energy confinement time accompanying pellet injection.

---

\* Present Address: Department of Physics, Auburn University, Auburn, Alabama.

† Present Address: Fusion Research Center, University of Texas, Austin, Texas.

‡ Present Address: Advanced Technology Engineering, Varian, Beverly, Massachusetts.

## Background and Motivation

Pellet fueling has been demonstrated [1] to result in improved global energy confinement in high density ( $\bar{n}_e > 3 \times 10^{20} m^{-3}$ ) ohmically heated plasmas in the ALCATOR C tokamak. This range of densities corresponds, for gas fueled discharges, to the so-called saturated confinement regime, in which energy confinement departs from the neo-Alcator scaling  $\tau \propto \bar{n}_e$  [2]. With pellet fueling, this degradation in confinement relative to the empirical scaling is not observed. At the highest densities,  $\bar{n}_e \approx 1 \times 10^{21} m^{-3}$ , the pellet fueled discharges have confinement times consistent with neoclassical ion transport and values of the confinement parameter,  $n_0 \tau_E$ , in excess of the Lawson criterion for thermalized breakeven.

Neither the relatively poor confinement in gas fueled discharges nor the improved performance with pellet injection has been satisfactorily explained. In particular, since at high density the electron and ion temperatures are closely coupled, it is not possible to determine unambiguously whether the improvement relative to gas-fueled discharges is due to reductions in electron or ion losses. Previous experiments in gas fueled discharges at lower density indicated the presence of anomalous ion thermal conduction loss [2]. An ion thermal diffusivity,  $\chi_i$ , roughly 3 to 5 times greater than the Chang-Hinton neoclassical prediction [3] was inferred from those results. Such an anomaly would be sufficient to account for the observed confinement behavior in higher density gas fueled plasmas. It is therefore natural to suppose that the beneficial effect of pellet injection is due to suppression of anomalous losses through the ion channel, perhaps through modification of the density or pressure profile. However, an increase in the electron thermal conductivity relative to the neo-Alcator value would also be consistent with the data. This interpretation [4] suggests an analogy to the appearance of enhanced electron losses in L-mode neutral beam heated tokamaks. The improved confinement in pellet fueled discharges might then be interpreted as a transition to H-mode resulting from a decrease in electron thermal conductivity.

To clarify the effect of pellet injection on electron and ion heat transport processes, we have carried out pellet injection experiments at moderate density ( $1 \times 10^{20} < \bar{n}_e < 3 \times 10^{20} m^{-3}$ ); for these parameters  $T_e$  and  $T_i$  are sufficiently separated for the electron and ion energy loss channels to be distinguished. Global energy confinement times in these

plasmas are typically in the "unsaturated" or electron dominated regime characterized by neo-Alcator scaling. We employ time-dependent transport analyses using the experimentally determined plasma parameters to obtain the variation of electron and ion thermal diffusivities during the discharge.

### Experimental

In the present experiments the ALCATOR C tokamak (major radius  $R=0.64$  m, minor radius  $a=0.165$  m) was operated at toroidal fields in the range  $8.0 \leq B_T \leq 10.0T$  with plasma current  $250 \leq I_p \leq 550kA$ . Frozen deuterium pellets were injected at  $\sim 600-800$  m/sec into ohmically heated  $D^+$  discharges by means of a four-shot pneumatic injector [5]. Two pellet sizes, with diameters of 1.0 and 1.5 mm, containing approximately  $3 \times 10^{19}$  and  $6 \times 10^{19}$  deuterium atoms respectively, were employed. The density of the target plasma was typically in the range  $1 < \bar{n}_e < 2.5 \times 10^{20}m^{-3}$ . Molybdenum limiters were employed throughout the course of these experiments.

Plasma current and one-turn voltage are monitored by standard magnetic diagnostics. Electron temperature profiles,  $T_e(r,t)$ , are obtained from second harmonic electron cyclotron emission (ECE) using scanning Fabry-Perot and grating instruments. Absolute calibration is derived from Thomson scattering and Soft X-ray pulse height analysis. Density profiles are measured using a 5-chord FIR laser interferometer; single time points are also obtained from Thomson scattering. Measurement of visible bremsstrahlung emission provides information on  $Z_{eff}$  and supplements the density profile data. The (d,d) neutron rate is determined from calibrated  $BF_3$  long counters and a bank of  $He^3$  detectors.

Figure 1 depicts a typical pellet injection shot. A single pellet is injected at about 310 msec, raising the line average density by approximately  $1.2 \times 10^{20}m^{-3}$ . As the plasma is diluted by cold particles from the pellet, the electron and ion temperatures decrease, leading to a drop in neutron rate and an increase in the resistive voltage. There is also a small decrease in total plasma current. On the fast time scale ( $\leq 1msec$ ) the total kinetic energy of the plasma is essentially unchanged. The plasma then re-heats in about 40 msec, as the line average density decays somewhat more slowly, reaching a quasi-steady value of  $3.0 \times 10^{20}m^{-3}$  after 90-100 msec. The final density is greater than that of the target

by about 25% in this case. For this example, both the neutron emission and the central electron cyclotron emission (second harmonic) show sawtoothing behavior before and after pellet injection.

The shape of the electron temperature profile is essentially the same before and after injection, although the peak temperature is reduced in the post-injection plasma. The density profile, on the other hand, becomes significantly more peaked following injection, as shown in figure 2, and relaxes slowly to a shape similar to that of the target gas-fueled plasma. This behavior may be seen more clearly in figure 3, which depicts the temporal behavior of the scale lengths  $a_{T_e}$ , the effective Gaussian width of the electron temperature profile, and  $r_n^{eff}$ , a measure of the density scale length related to the "peak-to-average ratio" and defined here by

$$r_n^{eff} = \int_0^a n(r) dr / n(0).$$

### Analysis Technique

The data analysis is carried out using a modified version of the ONETWO [6] transport code. Parameterized profiles of  $T_e(r)$  and  $n_e(r)$ , along with values of  $I_p$ ,  $V_R$ , and the measured neutron rate are supplied at up to 20 instants (time-slices) before and after the time of pellet injection.

The physical processes considered in the analysis include electron and ion heat transport, particle transport, magnetic diffusion, neutral transport, and radiation. The analysis is performed in 1-D geometry, assuming concentric circular flux surfaces. The relevant diffusion equations are

$$\frac{\partial n_e}{\partial t} = -\nabla \cdot \Gamma_e + S_e \quad (1)$$

$$\frac{3}{2} \frac{\partial n_e T_e}{\partial t} = \frac{1}{r} \frac{\partial}{\partial r} r (n_e \chi_e) \frac{\partial T_e}{\partial r} - \frac{5}{2} T_e \Gamma_e + P_\Omega - P_\Delta - P_{rad} \quad (2)$$

$$\frac{3}{2} \frac{\partial(\sum_i n_i)T_i}{\partial t} = \frac{1}{r} \frac{\partial}{\partial r} r \left( (\sum_i n_i) \chi_i \frac{\partial T_i}{\partial r} - \frac{5}{2} T_i (\sum_i \Gamma_i) \right) + P_\Delta - P_{CX} \quad (3)$$

$$\frac{\partial B_\theta}{\partial t} = \frac{\partial E}{\partial r} \quad (4)$$

Here,  $\Gamma_{e,i}$  are the electron and ion particle fluxes;  $S_e$  is the net (electron) source rate from all processes;  $\chi_{e,i}$  are the thermal diffusivities of electrons and ions, respectively;  $P_\Omega$  is the ohmic heating power density,  $(E \cdot j)$ ;  $P_\Delta$  is the electron-ion equilibration power;  $P_{rad}$  is the local radiated power density; and  $P_{CX}$  represents the charge-exchange loss term.

Boundary conditions for the electron temperature and density are taken from fits to the measured profiles. The ion temperature at the boundary is assumed equal to the local electron temperature. The boundary condition for the magnetic diffusion equation is obtained from the total plasma current.

A single impurity species, either carbon or oxygen, is assumed to be present, and the particle flux is taken to be ambipolar, *i.e.*

$$-\Gamma_e = \sum_i Z_i \Gamma_i. \quad (5)$$

The impurity temperature is taken equal to that of the hydrogenic ion species. The total source rate (Eq. 1) is obtained with the aid of a neutral transport package. An assumed global particle confinement time,  $\tau_p^{in}$ , provides the necessary boundary condition for this calculation. For the plasma parameters considered here, the results of the analysis are insensitive to the choice of this parameter. Radiated power (Eq. 2) is calculated for bremsstrahlung and line radiation due to the assumed impurity species.

For our purposes it is not necessary to model the internal particle source due to ablation of the pellet explicitly. Rather, an *ad hoc* source term  $S_{pel}$  is introduced which balances the observed  $\partial n / \partial t$  at the time of injection. This technique avoids numerical difficulties associated with the very rapid flows immediately after injection.

The magnetic diffusion equation is solved assuming classical resistivity and using  $I_p(t)$  as the boundary condition.  $Z_{eff}$  is adjusted to match the experimental loop voltage and the resulting value compared with that determined by the visible Bremsstrahlung diagnostic for consistency. The shape of the  $Z_{eff}$  profile is adjusted over a narrow range to provide consistency between the computed value of the axial safety factor  $q_0$  and the presence or absence of sawteeth in the discharge. Since the experimental inputs are averaged over sawtooth periods, no explicit effects of internal disruptions are included in the time-dependent analysis. The time-averaged effects of sawteeth on the central energy and particle balance are therefore included in the inferred values of the transport coefficients.

The ion heat transport equation is solved assuming an ion thermal diffusivity of the form

$$\chi_i = W \times \chi_i^{Neoc} + D_b f(q)$$

where  $\chi_i^{Neoc}$  is the Chang-Hinton neoclassical coefficient,  $D_b$  is the Bohm diffusivity and

$$f(q) = 1 - \frac{1}{1 + (1/q - 1)^2} \quad q \leq 1$$

models the time-averaged effect of sawtooth activity. The time dependent anomaly factor  $W(t)$  is dynamically adjusted to reproduce the observed neutron emission rate using a "feedback" procedure

$$\frac{dW}{dt} = G_1 \left( \frac{R_n^{exp} - R_n^{code}}{R_n^{exp}} \right) + G_2 \frac{d}{dt} \left( \frac{R_n^{exp} - R_n^{code}}{R_n^{exp}} \right)$$

where  $R_n^{exp}$  is the experimentally observed neutron rate and  $R_n^{code}$  is the rate predicted by the code. The gains  $G_1$  and  $G_2$  are chosen to avoid numerical instability. A similar procedure is used to adjust  $Z_{eff}$  to obtain the correct voltage when solving the magnetic diffusion equation.

## Results

Pre-pellet plasmas typically exhibit values of ion thermal conductivity a factor of three to five higher than neoclassical. This trend is apparent over a wide range of parameters,

and confirms earlier work [2] which concluded that significant anomalous ion losses were present. Following pellet injection the anomaly factor typically decreases to order unity, as shown in the time history in figure 4. In this example, the improvement persists for  $\sim 60$  msec, following which a significant anomaly reappears. The inferred value of  $\chi_i$  at the half radius falls from  $\sim 0.5 m^2/sec$  before the pellet to less than  $0.1 m^2/sec$  at 50 msec after injection. Variation of the ion thermal diffusivity before and after pellet injection for a range of plasma currents is shown in figure 5. The improvement is consistent and persists for between 20 and  $> 100$  msec in different discharges.

While ion thermal transport decreases following pellet injection, the electron thermal conductivity  $\kappa_e$  in general either remains constant or increases somewhat according to the code results. The increase in these cases however may be artificial, since the radiation losses included in these code runs are the result of a calculation based on a single, low Z impurity species, rather than on bolometric measurements. It is therefore possible that increased radiation loss at the higher density following injection is being incorrectly attributed to electron thermal conduction. The uncertainties in the electron transport are thus more severe than for the ions. Values of the electron thermal conductivity corresponding to the ion data in figure 5 are shown in figure 6. From neo-Alcator scaling we would expect  $\kappa_e$  to be independent of density, and therefore unchanged following pellet injection. If the increases shown are not due to errors in the modelling, they may result from an unfavorable dependence on  $\nabla n$ , which might be expected for drift wave transport. However, because of the uncertainty noted above, no strong conclusions on this point can be drawn from the present data, beyond the qualitative observation that, in contrast to the ions, electron losses do not in general decrease following pellet injection.

The most apparent difference between the pellet- and gas- fueled discharges in terms of directly measured experimental quantities is the more peaked density profiles typical of the post-injection plasmas. We note that the temporal behavior of the ion anomaly depicted in figure 4 is similar to the evolution of the density profile width  $r_n^{eff}$  for this shot (figure 3). In figure 7 we plot these quantities for a different shot, in which the peaking of the density profile persists for several hundred msec. The qualitative similarity of the two traces is also evident in this case, suggesting a correlation between the shape of the

density profile and the mechanism for the anomalous ion loss. A plot of  $\chi_i/\chi_{Neo}$  vs.  $r_n^{eff}$  for a collection of data is shown in figure 8, and does indicate at least a weak correlation. However, the large scatter in the data may imply that the "proper" scaling variable for the ion anomaly is more complicated than the simple global quantity  $r_n^{eff}$ . The fact that several of the points in figure 8 correspond to anomaly factors less than one is consistent with the estimated errors discussed in the following section.

### Error Sensitivity

Because the difference between  $T_e$  and  $T_i$  is small, particularly after the pellet is injected, there are necessarily significant uncertainties in the values of the transport coefficients resulting from our analysis. We have conducted sensitivity studies to assess the reliability of our results.

The principal experimental uncertainties arise from the accuracy of the measurement of  $T_e$  and the density profile. The error in the central electron temperature is estimated, from comparison of calibrations due to soft X-ray and Thomson scattering techniques and from shot to shot variation over similar discharges, to be of the order of 10%. The width of the  $T_e$  profile is typically measured to similar accuracy. The error in the line integral of the density as measured by the sub-millimeter interferometer is less than  $\pm 5\%$  for densities in the range  $1 \times 10^{20} \leq \bar{n} \leq 3 \times 10^{20} m^{-3}$ . However, the Abel transform required to obtain local  $n_e(r)$  introduces errors and the approximation by a three parameter standard profile used in the code further degrades the accuracy. We estimate a 15% error bar on  $n_e(0)$  to be reasonable. This estimate is supported by comparison with Thomson scattering data. The error in the calibration of the absolute neutron rate is less than 25%, which has little impact on the implied ion temperature.

The results of varying parameters within these error estimates on the evaluation of the neoclassical multiplier are shown in figure 9. Each trace represents a code run based on the shot depicted in figure 7 but with different input values corresponding to assumed errors in calibration or profile determination. The pre-pellet discharge is clearly inconsistent with neoclassical ion transport in all cases, while the post-injection values are all below  $\chi_i/\chi_{Neo} = 1.5$ . Some of the runs lead to anomaly factors less than unity following injection.

The relatively larger spread in the post-pellet traces is, of course, due to the closer coupling between electrons and ions and the reduction in  $(T_e - T_i)$ .

In the above, errors in calibration have been assumed to be consistent throughout the discharge. In the case of the density profile, particularly, it is also important to consider the effect on the analysis of possible time dependent errors. This is especially true in light of the apparent correlation between the evolution of the density profile and anomalous transport illustrated in figures 3,4, and 7. The possibility that this correlation could be an artifact of the analysis technique was tested by re-doing the analysis of the data of figure 7 using a false  $n_e(r, t)$  profile such that  $\bar{n}_e(t)$  was unchanged, but the time history of  $r_n^{eff}(t)$  after injection more closely resembled that of figure 3, i.e. first decreasing and then returning close to its pre-pellet value. The resulting behavior of the inferred anomaly factor for this case is included in figure 9 and is essentially indistinguishable from the nominal value. We may therefore conclude that the relationship between density profile and ion transport is valid and not a consequence of implicit dependences inherent in the analysis.

### Discussion

It is apparent from the data that the gas fueled plasmas exhibit significant anomalies in ion thermal diffusivity which are reduced following pellet injection. Furthermore the effect appears to be related to the peaking of the density profile, although the "effective profile width"  $r_n^{eff}$  may not be the best scaling parameter when applied to a range of discharges. In particular, we note that the gas fueled cases in figure 8 show no positive correlation with profile width. Nevertheless, we are led to consider anomalous transport mechanisms which depend directly or indirectly on the density profile.

In applying the results of our analysis to any such mechanism, it is necessary to consider several points. First, in the absence of measured profiles for the ion temperature, the analyses have been carried out under the assumption that the anomalous ion conduction is of the form of a constant multiplier times the neoclassical coefficient. There is, of course, no valid basis for such a model, and specific anomalous transport models may in fact scale quite differently. The self-consistent  $T_i(r, t)$  generated by the code will therefore not correspond to that resulting from an alternative model with the same "average" effects.

This fact is important for mechanisms which depend on the ion temperature profile, for example. Further, the values of  $\chi_i$  at particular locations can not be directly compared with theoretical predictions with different spatial dependences. Another difficulty arises from the reduction of experimental data to simplified analytic forms for use in the code. While the parameterization is adequate for the calculation described, as evidenced by the relative insensitivity of the results to artificial variations in the profiles, it is not sufficiently detailed to give accurate values for gradients, for example. Use of these forms in conjunction with models which depend on local scale lengths, *e.g.* of the density and temperature, may produce unreliable results.

Keeping these considerations in mind, we nevertheless may examine our data in the context of some specific mechanisms, looking for general trends rather than precise agreement. One possible effect which bears at least qualitative similarities to the experimental results is the ion mixing mode [7]. Here the relevant parameter is the quantity

$$\eta_i = \frac{d \ln T_i}{d \ln n_i},$$

the ratio of the ion density and temperature scale lengths. The mode is unstable for large values of  $\eta_i$  and can lead to anomalous ion heat loss. An approximate form [7] for the critical value for stability in the collisionless limit is

$$\eta_{crit} \approx \frac{1}{2} [1 + (1 + 113 (\frac{r_n}{Rq})^2)^{1/2}]$$

where  $r_n = (d \ln n / dr)^{-1}$  is the local density scale length. While there is no correlation between  $\chi_i / \chi_i^{Neo}$  and the ratio  $\eta_i / \eta_{crit}$ , as shown in figure 10, it is interesting that the values of  $\eta_i / \eta_{crit}$  for both pellet and gas fueled cases lie close to unity, easily within the combination of experimental and modeling error and theoretical uncertainty. While this result may be purely coincidental, it might be conjectured that the thermal transport due to these modes has the effect of flattening the ion temperature profile sufficiently to reduce  $\eta_i$  to the marginally stable value; effective saturation of the mode would therefore occur at an amplitude corresponding to the self-consistent enhancement of  $\chi_i$ . Simulations based on the estimated thermal diffusivity contained in [7] indicate that the transport is sufficiently

large to produce this result, while simulations with only neoclassical ion transport lead to values of  $\eta_i \gg \eta_{crit}$  over much of the plasma for the pre-injection case. On the other hand, more recent theoretical work [8,9] on the non-linear saturation of the mixing mode may lead to smaller values of the saturated amplitude and the corresponding anomalous transport.

While the clearest difference between gas and pellet fueled discharges is their density profiles, they are not identical in all other respects and we cannot rule out other causes for the improved ion confinement. For example, the lack of intense gas puffing in pellet discharges may change the power balance in the discharge edge. Further, the differences in the density profiles reflect differences in particle transport and while we can recognize correlations between energy and particle transport, cause and effect are more difficult to sort out.

### Conclusions

We have confirmed the presence of significant excess ion thermal losses in gas fueled ohmic discharges in the density range  $10^{20} \leq \bar{n}_e \leq 3 \times 10^{20} m^{-3}$  and currents  $250 \leq I_p \leq 550 kA$ . The ion heat flux corresponds to a thermal diffusion coefficient 3 to 5 times the Chang-Hinton neoclassical value. Following pellet injection the ion thermal diffusivity at the half-radius decreases from values near  $0.5 m^2/sec$  to near  $0.1 m^2/sec$ ; the latter correspond to neoclassical predictions for these plasma parameters. While the ion thermal conductivity  $\kappa_i$  typically falls in these cases,  $\kappa_e$  appears to rise or remain roughly constant.

In some instances the neoclassical level of ion transport persists throughout the remainder of the discharge. More typically, the ratio of  $\chi_i/\chi_i^{Neo}$  increases with time and may approach the pre-injection value. The behavior of the anomaly factor for a given discharge is strongly correlated with the peaking of the density profile, and some correlation between the global parameter  $r_n^{eff}$  and the anomalous diffusivity is apparent from the data. The values of  $\eta_i$  obtained are close to the critical values for marginal stability for the ion mixing mode. One may speculate that the large spread in ion thermal conductivity observed corresponds to that required to sufficiently flatten the ion temperature profile as to provide stability with respect to a given density profile.

The typical magnitude of the anomalous ion transport in the gas fueled target plasmas in this parameter range corresponds to  $\chi_i^{anom} \approx 0.4 m^2/sec$ . The presence of an anomalous thermal diffusivity of this magnitude in higher density discharges would be sufficient to account for the observed saturation in global energy confinement in gas fueled ALCATOR C plasmas. Moreover, the lack of saturation in the best high density pellet fueled cases, which also exhibited the strongest peaking of the density profile, is consistent with the effect documented here. Therefore, while the present work cannot unambiguously account for the high density results, it suggests that a similar mechanism is responsible.

### Acknowledgements

The authors wish to thank the ALCATOR C operating team and technical staff for their invaluable contributions to this work. We are also grateful to R. Englade and P. Diamond for helpful discussions regarding the ion mixing mode. This work was supported by the United States Department of Energy, Contract No. DE-AC02-78ET-51013.

## References

- [1] GREENWALD, M., GWINN, D., MILORA, S., PARKER, J., PARKER, R., *et al.*, Phys. Rev. Lett. 53, 352 (1984).
- [2] PARKER, R.R., Bull. Am. Phys. Soc., 27, 986 (1982); ALCATOR GROUP, "ALCATOR C Status and Program Plan," MIT Report PFC/IR-82-3, (December, 1982).
- [3] CHANG, C.S. and HINTON, F.L., Physics of Fluids 25, 1493 (1982).
- [4] GOLDSTON, R., Plasma Physics and Controlled Nuclear Fusion 26, 87 (1984).
- [5] MILORA, S.L., Journal of Fusion Energy, 1, 15 (1981).
- [6] PFEIFFER, W.W., DAVIDSON, R.H., MILLER, R.L., and WALTZ, R.E., "ONETWO: A Computer Code for Modelling Plasma Transport in Tokamaks" GA-A16178, (1980).
- [7] ANTONSEN, T., COPPI, B., and ENGLADE, R., Nuclear Fusion 19 (1979) 641.
- [8] DIAMOND, P., Private Communication (1985).
- [9] ENGLADE, R., COPPI, B., and MIGIUOLO, S., "Heat Transport Due to Ion Mixing Modes," Sherwood Theory Meeting Paper 2Q20, Madison, Wisconsin (1985).

## Figure Captions

- Figure 1. Variation of plasma parameters during a typical pellet injection shot. The resistive voltage is obtained from the measured surface voltage by accounting for the change in magnetic energy using a simple model of the current density profile. Line average density is measured by the central chord of a FIR interferometer. Second harmonic electron cyclotron emission from the plasma center is proportional to the central electron temperature. The deuterium pellet is injected at approximately 310 msec.
- Figure 2. Density profiles before and after pellet injection, as determined by Abel inversion of data from a five-chord FIR interferometer.
- Figure 3. Evolution of density and electron temperature width during the pellet injection shot depicted in Fig. 1. The temperature profile is essentially unchanged by the pellet, while the density profile undergoes an initial transient, then peaks, and finally relaxes to its original shape.
- Figure 4. Evolution of the anomaly factor with respect to neoclassical ion conduction inferred by the transport code for the shot depicted in Fig. 1-3.
- Figure 5. Inferred value of the ion thermal conduction anomaly before and after pellet injection for several currents. The post-pellet values are taken 30-50 msec after injection.
- Figure 6. Electron thermal conductivity evaluated at the half-radius before and after injection. The calculation of  $\kappa_e$  includes uncertainties in the radiated power term.
- Figure 7. Evolution of the density profile width and ion thermal conduction anomaly for a shot with no sawtooth activity following injection.
- Figure 8. The ion conduction anomaly plotted as a function of the density profile width. Post-pellet values include data up to 200 msec following injection.
- Figure 9. Results of a series of code runs based on the same shot as Fig. 8, but with parameters varied within limits of experimental error. The most extreme cases (labeled 893 and 894) correspond to variation of the electron temperature by  $\pm 10\%$ . The case labeled 900 was run using a false density profile with an effective width which behaved similar to that in Fig. 3 as a function of time. The result is essentially indistinguishable from the nominal case (880).
- Figure 10. The ion anomaly plotted as a function of the ratio  $\eta_i/\eta_{crit}$  evaluated at the half-radius,

using ion temperature profiles obtained from the code results.

10/11/84

SHOT # 67

B= 9.0 TESLA

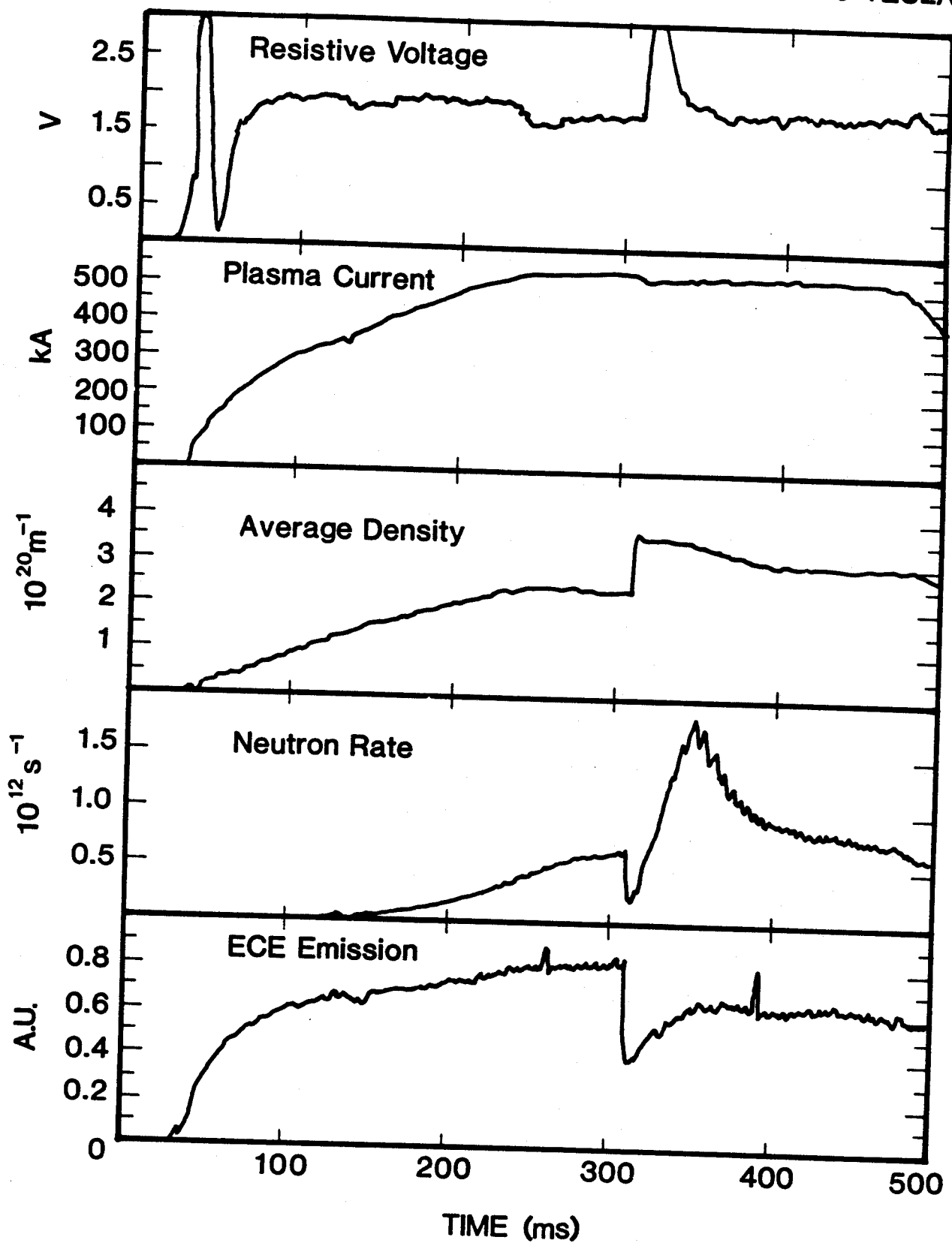


FIGURE 1

DENSITY PROFILE SHOT # 67 10/11/84

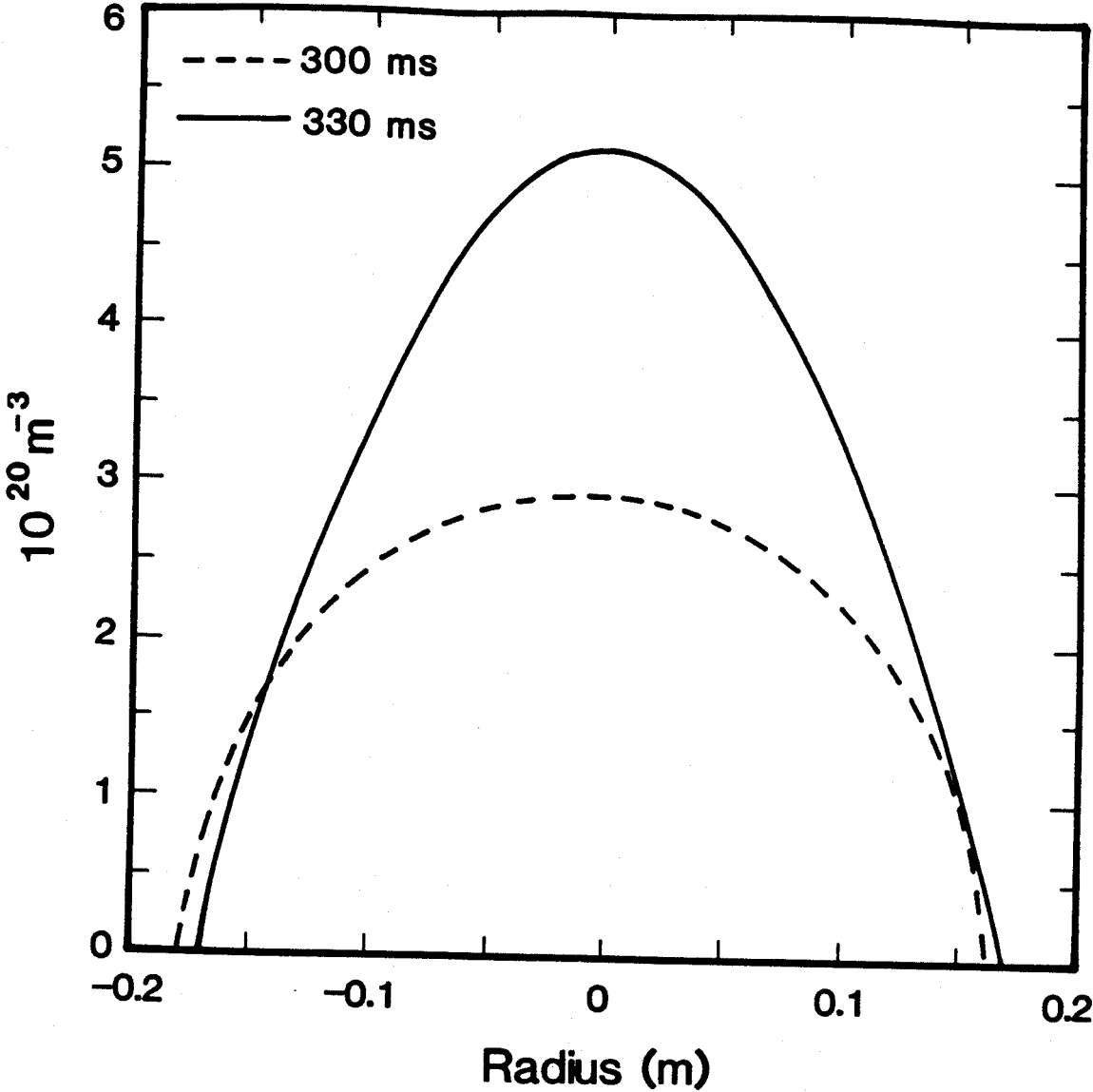


FIGURE 2

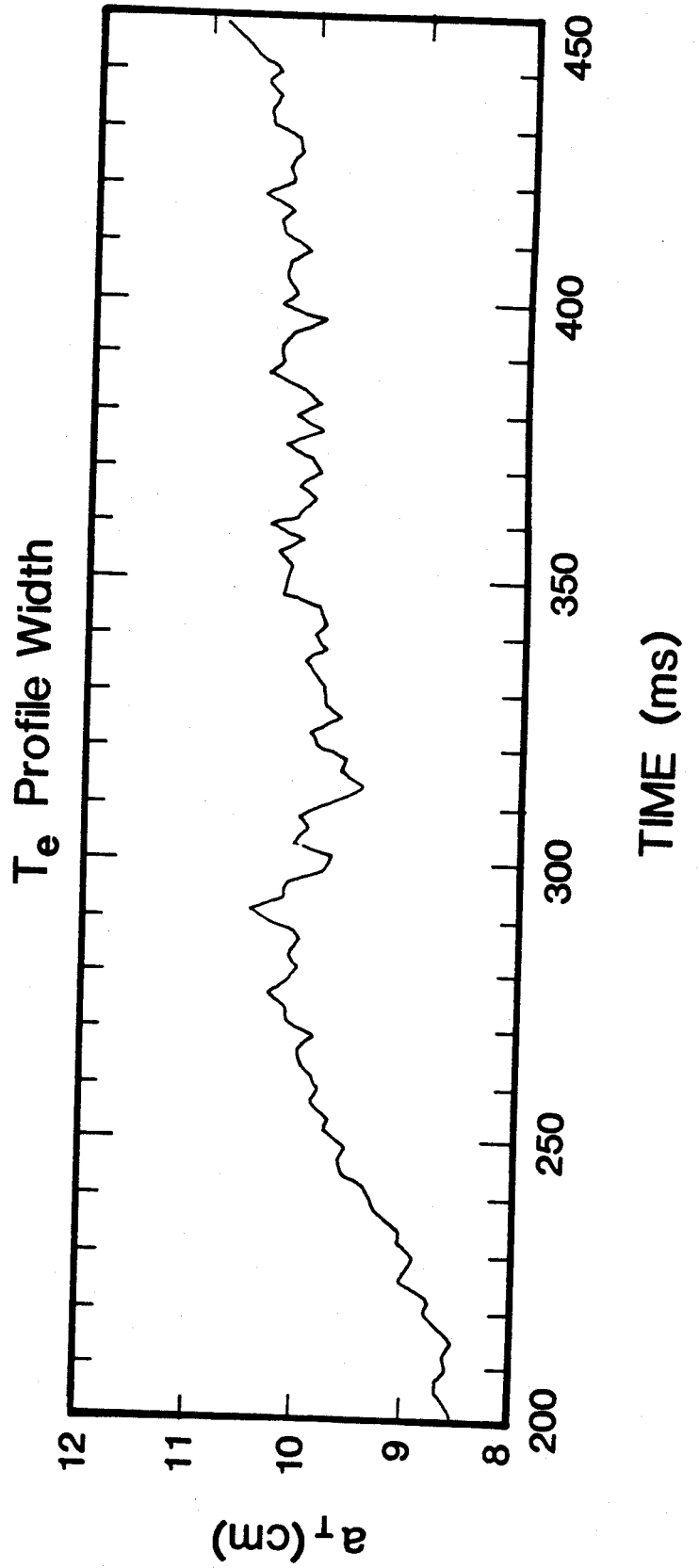
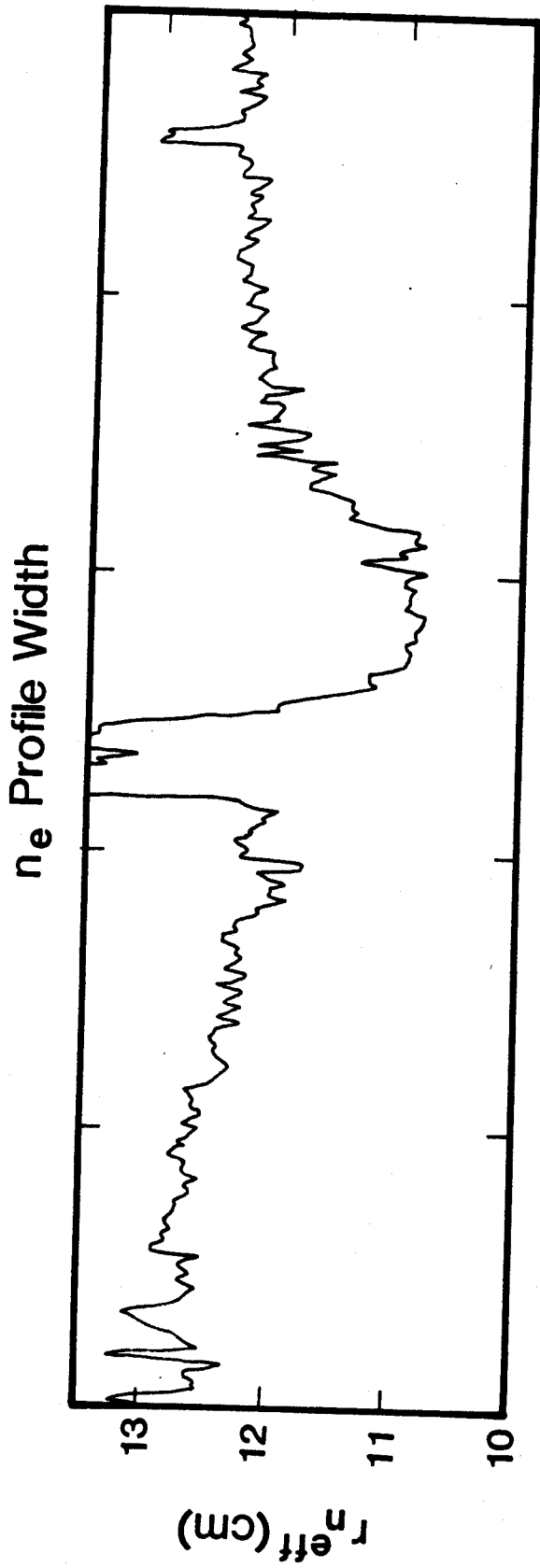


FIGURE 3

# NEOCLASSICAL MULTIPLIER

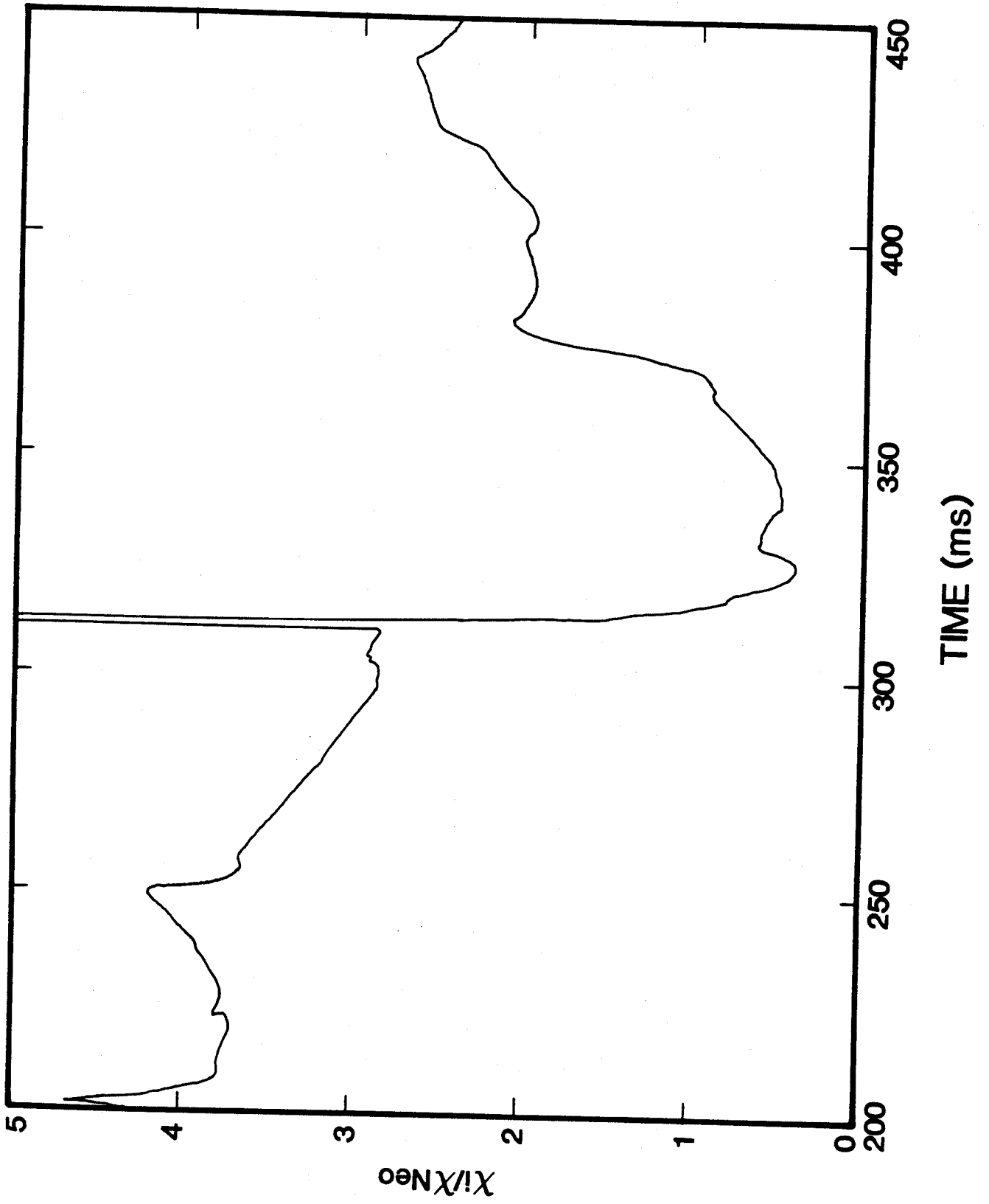


FIGURE 4

# ION ANOMALY vs PLASMA CURRENT

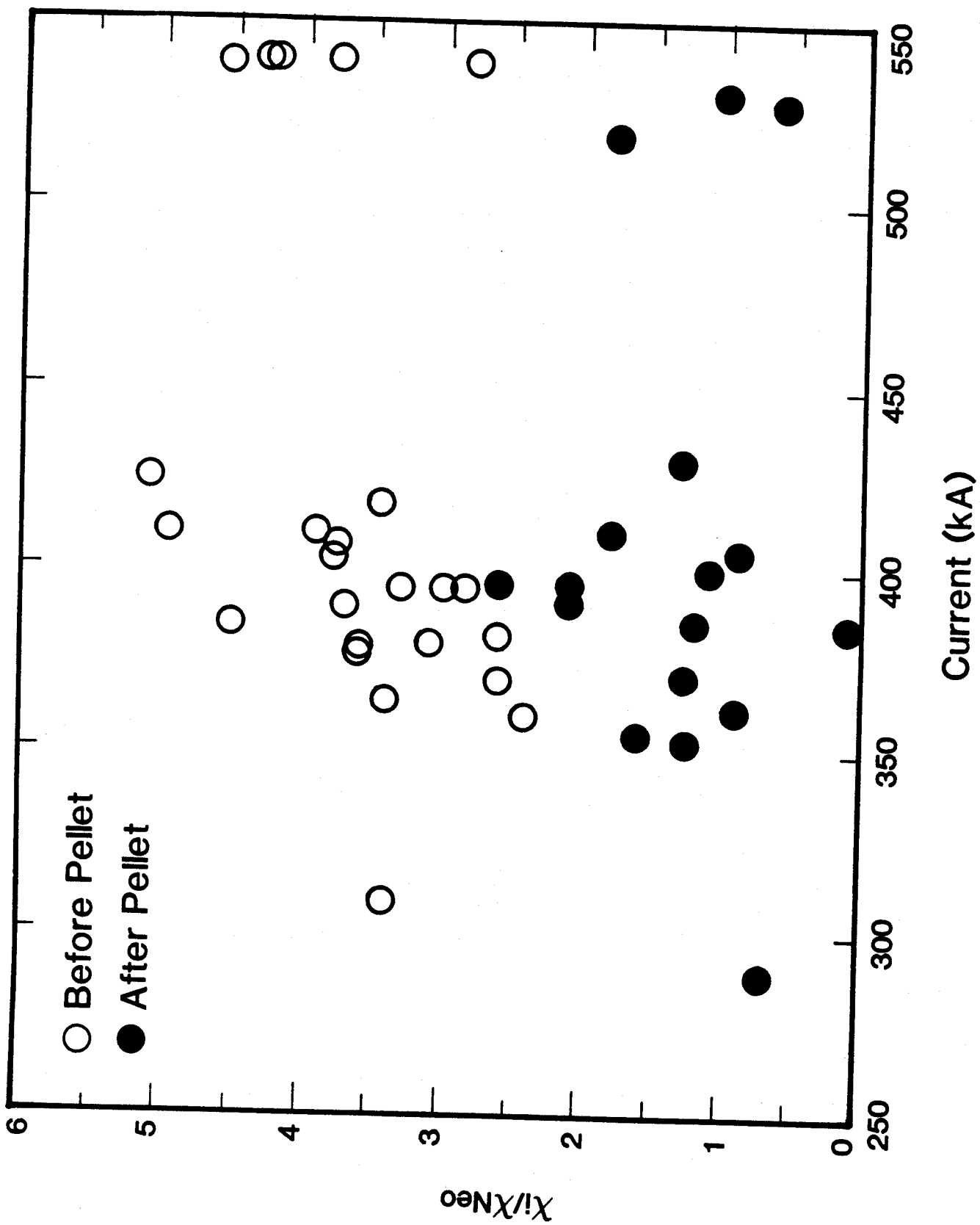


FIGURE 5

# ELECTRON THERMAL CONDUCTIVITY

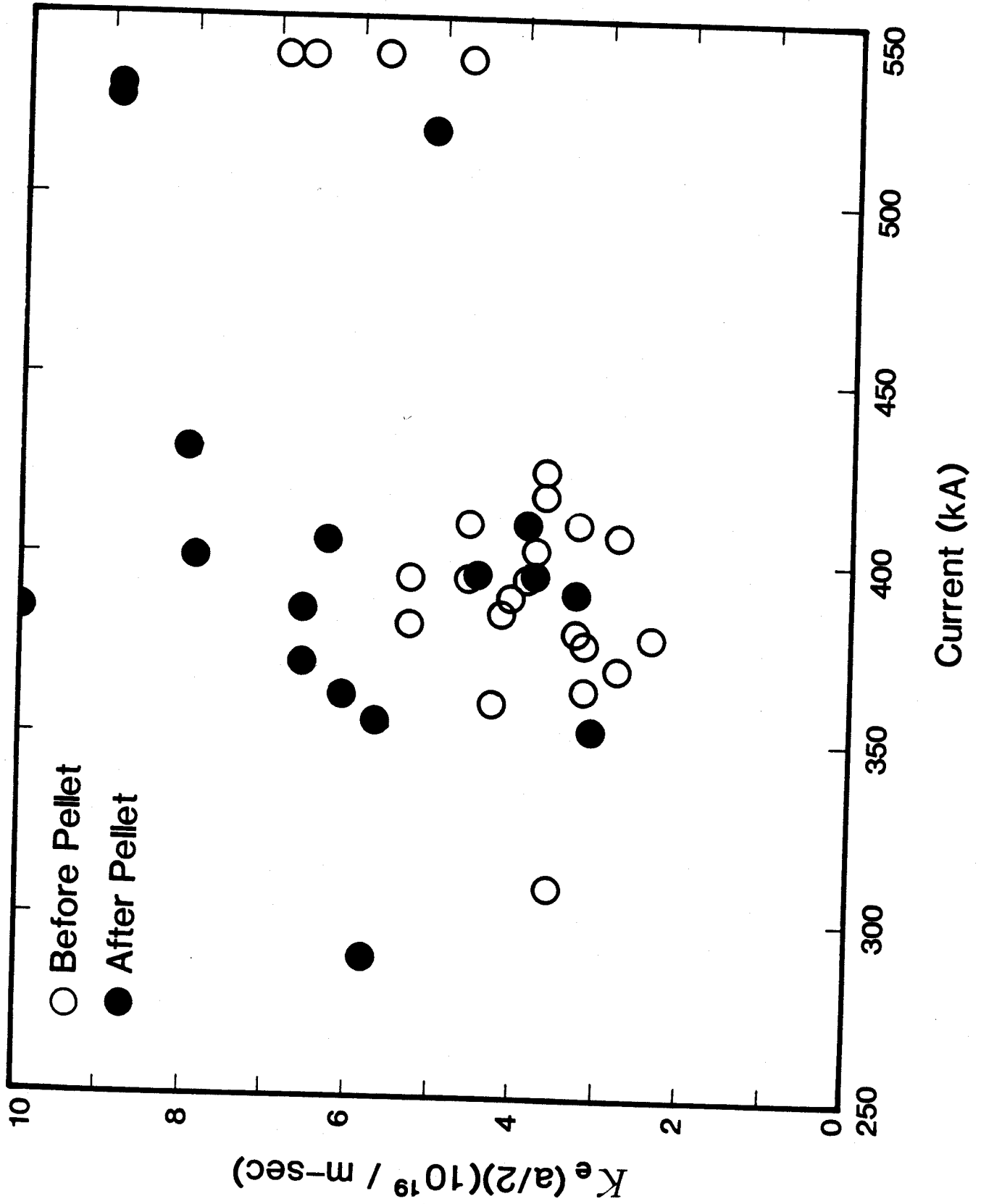


FIGURE 6

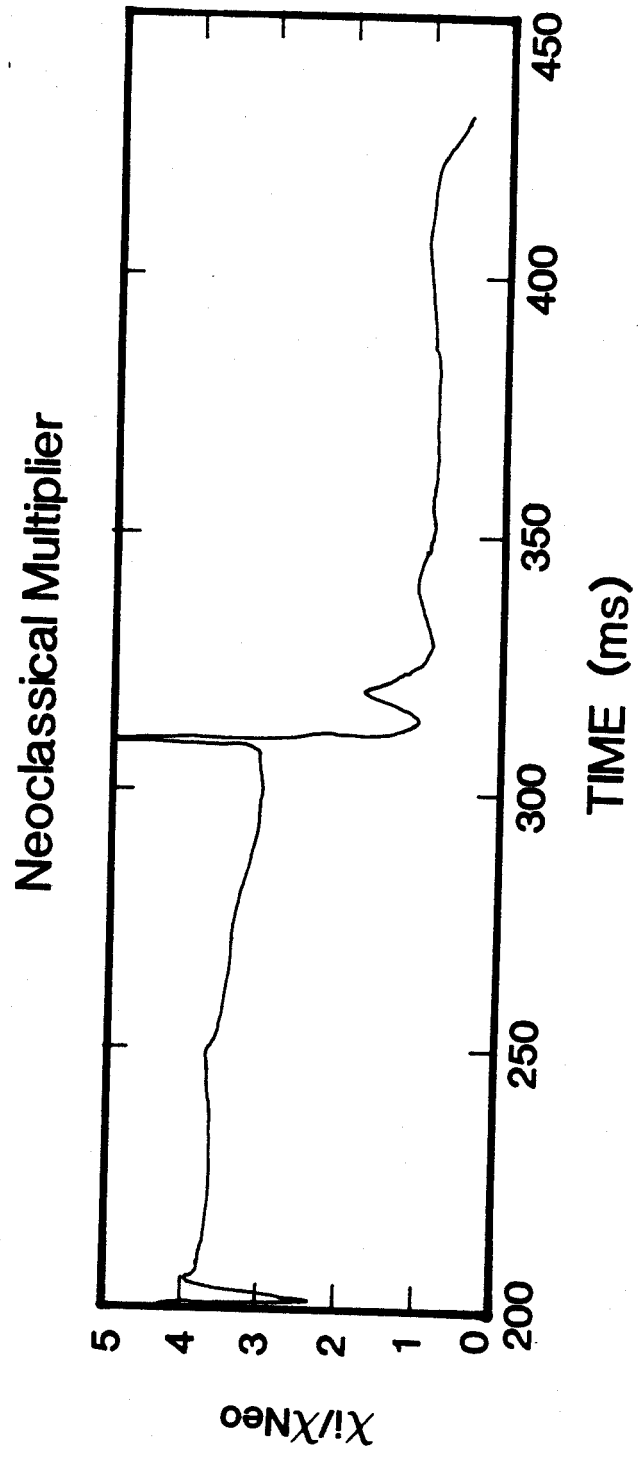
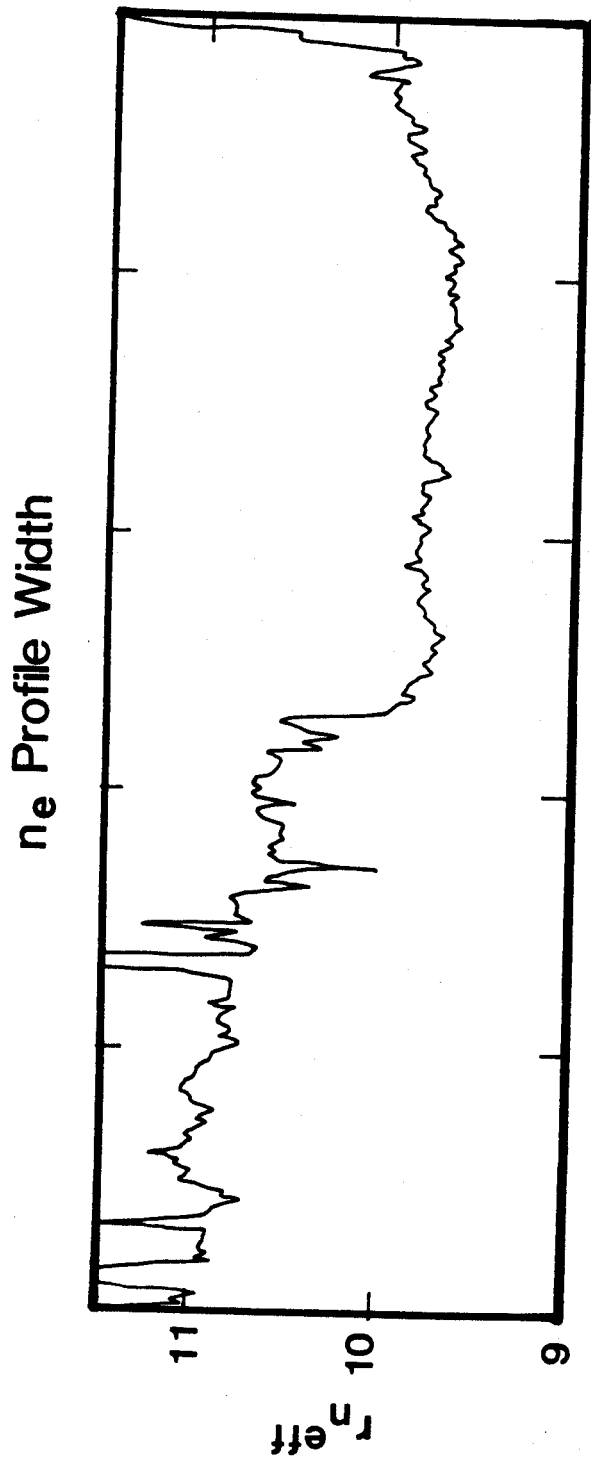


FIGURE 7

# ION ANOMALY vs DENSITY PROFILE

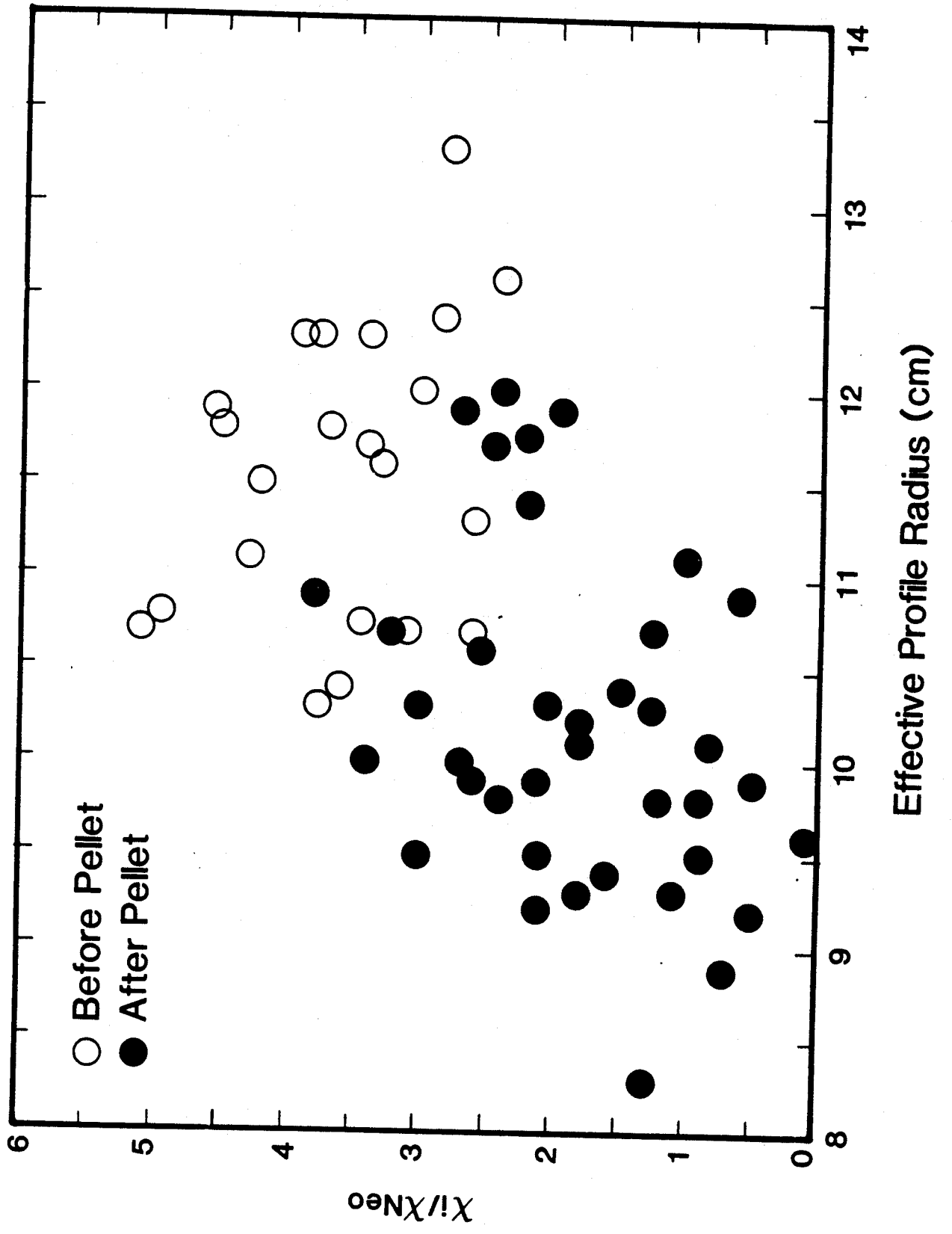


FIGURE 8

# NEOCLASSICAL MULTIPLIER

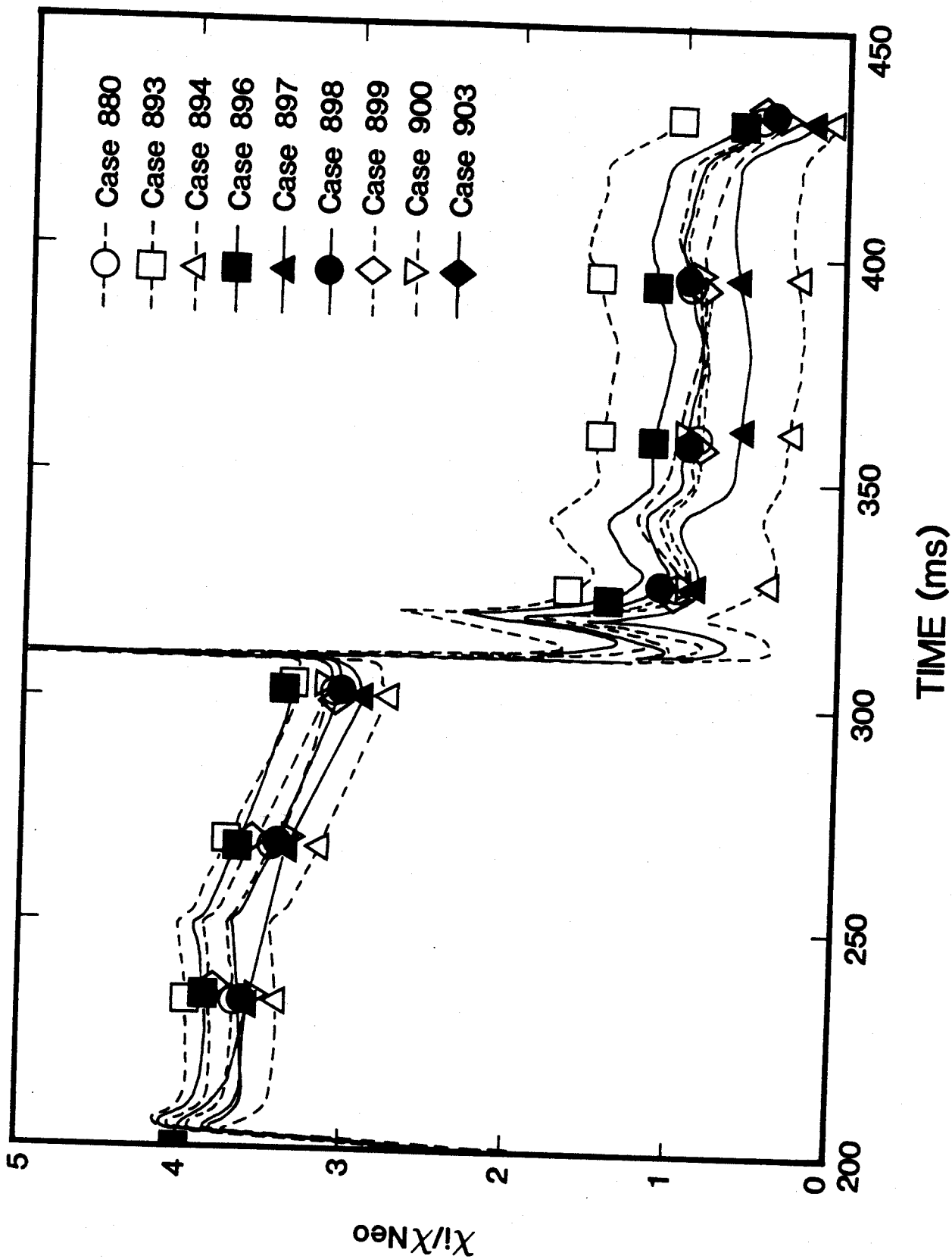


FIGURE 9

# ION ANOMALY vs $\eta_i/\eta_c$

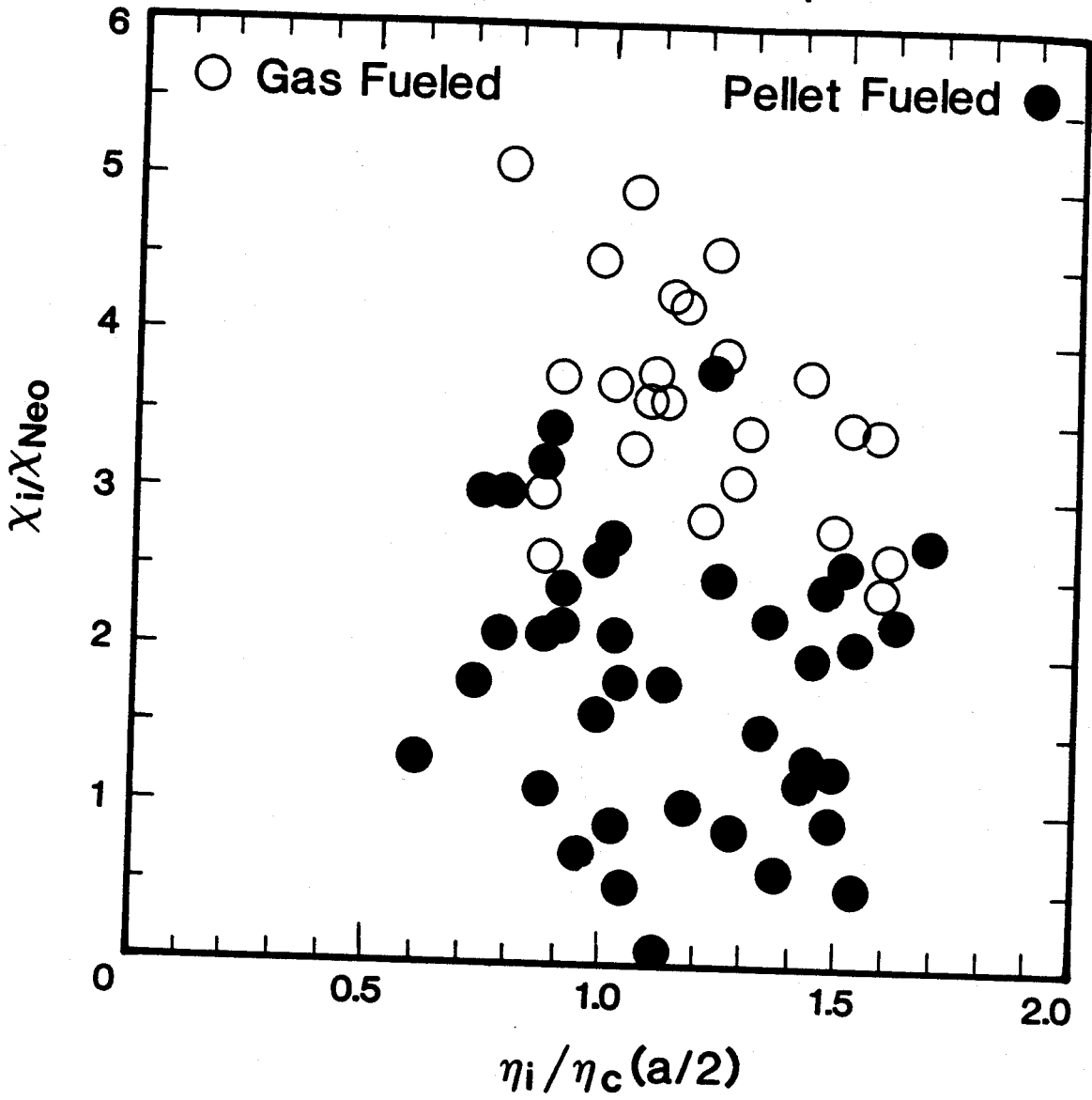


FIGURE 10